 doi:10.20944/preprints202201.0262.v1

Article

Compact Midwave Imaging System: Results from an Airborne Demonstration

Michael A. Kelly [1]*, James L. Carr [2], Dong L. Wu [3], Arnold C. Goldberg [1], Ivan Papusha [1], Renee Meinhold [1]

[1] Johns Hopkins University/Applied Physics Laboratory, 11100 Johns Hopkins Rd, Laurel MD 20723, USA
[2] Carr Astronautics, Greenbelt MD 20770; jcarr@carrastro.com
[3] NASA Goddard Space Flight Center; Greenbelt, MD 20770, USA, dong.l.wu@nasa.gov
* Correspondence: michael.kelly@jhuapl.edu; Tel.: +1-240-228-0788

Abstract: The Compact Midwave Imaging System (CMIS) is a wide field of view, multi-angle, multi-spectral pushframe imager that relies on the forward motion of the satellite to create a two-dimensional (2D) image swath. An airborne demonstration of CMIS was successfully completed in January-February 2021 on the NASA Langley Research Center Gulfstream III. The primary objective of the four-flight campaign was to demonstrate the capability of this unique instrument to perform stereo observations of clouds and other particulates (*e.g.* smoke) in the atmosphere. It is shown that the midwave infrared (MWIR) spectral bands of CMIS provide a unique 24/7 capability with high resolution for accurate stereo sensing. The instrument relies on new focal plane array (FPA) technology, which provides excellent sensitivity at much warmer detector temperatures than traditional technologies. This capability enabled a compact, low-cost design that can provide atmospheric motion vectors and cloud heights to support requirements for atmospheric winds in the 2017-2027 Earth Science Decadal Survey. Applications include day/night observations of the planetary boundary layer, severe weather, and wildfires. A comparison with current space-based earth science instruments demonstrates that the SWIR/MWIR multi-spectral capability of CMIS is competitive with larger, more expensive instrumentation. Imagery obtained over a controlled burn and operating nuclear power plant demonstrated the sensitivity of the instrument to temperature variations. The system relies on a mature stereoscopic imaging technique applied to the same scene from two independent platforms to unambiguously retrieve atmospheric motion vectors (AMVs) with accurate height assignment. This capability has been successfully applied to geostationary and low-earth orbit satellites to achieve excellent accuracy. When applied to a ground-point validation case, the accuracy for the CMIS aircraft observations was 20 m and 0.3 m/s for cloud heights and motion vectors, respectively. This result was confirmed by a detailed error analysis with analytical and covariance models. The results for CMIS cases with underflights of Aeolus, CALIPSO and Aqua provided a good validation of expected accuracies. The paper also showed the feasibility of accommodating CMIS on CubeSats to enable multiple instruments to be flown in a leader-follower mode.

Keywords: Stereo winds; cloud motion vectors; midwave infrared; weather satellite

1. Introduction

Atmospheric motion vectors (AMVs) have long provided an important component of the global observing system for tropospheric winds [1]. The 2017-2027 Earth Science Decadal Survey (ESAS 2017) [2] identified 3D winds including AMVs as a "targeted observable" to advance research objectives in atmospheric dynamics, severe weather, wildfire, and hydrology. The community increasingly recognizes that study of atmospheric dynamics is essential to the understanding of cloud-climate and cloud-precipitation processes, as discussed in the recommendation: "Global measurements of the spatiotemporal (four-dimensional) evolution of large-scale horizontal wind vectors are urgently needed" [3]. The Compact Midwave-Infrared Imaging System (CMIS) project is an effort to address these objectives with a compact, low-cost sensor that enables flexible accommodation on

Preprints (www.preprints.org) | NOT PEER-REVIEWED | Posted: 18 January 2022 doi:10.20944/preprints202201.0262.v1

CubeSat or as hosted payloads on small satellites. CMIS employs a robust stereo technique with accurate height assignment [4] to provide wide field of view (FOV), multi-angle observations of AMVs during the day and night over cloud-covered regions of the Earth (more than 60% coverage of the globe). This capability would produce vector winds resolved in 3D along each orbit, effectively complementing clear-air wind measurements yielded by LIDAR, to achieve a synergistic architecture for a global 3D wind characterization.

Until recently, only cryogenically cooled detector technologies such as InSb and HgCdTe, which require detector temperatures < 80 K were available for midwave infrared (MWIR) sensing. The detectors from CMIS are made from the newly available and continually improving high-operating temperature (HOT) MWIR detector technology based on Type II Superlattice (T2SL) detector structures. These detectors are able to deliver similar performance at operating temperatures near 150 K as those made from the incumbent InSb and HgCdTe technology. The significant increase in operating temperature allows for smaller, lighter and lower-power Stirling cycle coolers which are consistent with the resources available from a CubeSat. This paper presents the initial results of an airborne flight test carried out in early 2021, as well as provides a brief description of the CMIS design. The paper also describes how CMIS could provide a low-cost option for a future space mission.

2. Materials and Methods

2.1. Instrument

CMIS is a pushframe imager that relies on the forward motion of the satellite (or aircraft) to create a two-dimensional (2D) image swath. The optical design of pushframe imagers is based on a set of passband filters inserted into the optical path directly over a focal plane array (FPA) such that each filter strip maps into a unique row (line), or a continuum of rows (lines), on the array (see the colored stripes in the passband filter in Figure 1). A given wavelength strip on the filter covers >30 lines of pixels on the FPA at the same wavelength in order to allow for time-delay integration (TDI) to build up signal for dim targets. As the satellite moves along its orbital track, the nadir-looking imager takes samples of pixels in a cross-track swath and maps each pixel to a unique spot on the ground. In essence, each stripe on the filter (and thus each wavelength) images a different continuous ground swath at a given time. An instrument with a 512-km, along-track field of view hosted on a satellite in low-earth orbit and moving at a speed of ~7.5 km s^{-1} [5] would take approximately 68 s to acquire every stripe along the same ground swath.

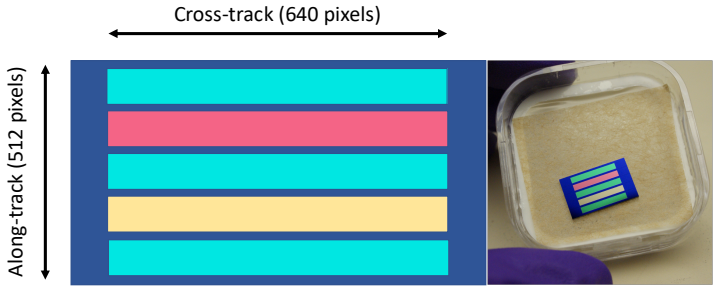

(**a**) (**b**)

Figure 1. (a) Stripe filter configuration for fore, nadir and aft views at 3.75 um for stereo imaging with bands at 4.05 and 2.25 μm for multispectral analysis. (b) Stripe filter for the Compact Midwave Imaging System.

Figure 2 presents the three spectral bands chosen for the CMIS instrument, superimposed on a MODTRAN atmospheric transmission spectrum. The bands are located in

Preprints (www.preprints.org) | NOT PEER-REVIEWED | Posted: 18 January 2022 doi:10.20944/preprints202201.0262.v1

spectral windows where the atmosphere has high transmission. The band at 3.75 μm provides day and night (24/7) images at a higher spatial resolution than can be obtained with LWIR sensor on a pixel-by-pixel basis for the same size of lens due to the smaller diffraction blur at shorter wavelengths. The band at 4.05 μm can be used to derive temperatures, including those for land and sea surfaces, volcanic plumes and wildfires. Finally, the band at 2.25 μm, which is dominated by solar reflection, provides high-spatial-resolution cloud reflectivity data that will aid in the determination of AMVs, cloud/surface phenomenology discrimination and removal of the daytime solar signal from the 4.05-μm band. The SWIR band is also useful for detecting hot wildfires with fewer saturated pixels than MWIR bands, due to blackbody physics and narrow bandwidth.

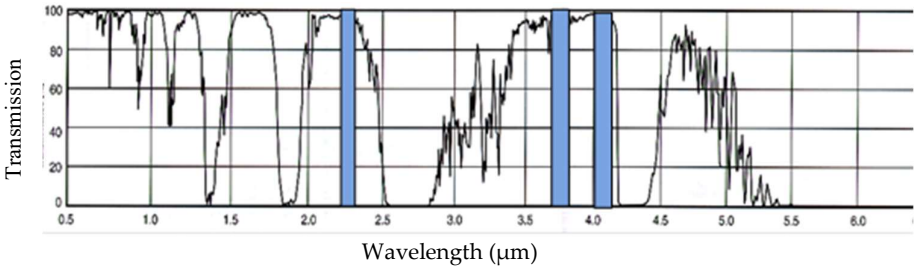

Figure 2. The CMIS bands (blue shaded) area superimposed on a MODTRAN atmospheric transmission spectrum.

The utility of a 3.75-μm band can be better understood as follows. The Visible Infrared Imaging Radiometer Suite, onboard the Suomi NPP satellite, has an improved resolution of 750-m ground sample distance with respect to the 1000-m GSD of the Moderate Resolution Imaging Spectroradiometer (MODIS) for the 3.75- and 12-μm channels, which results in higher precision for retrieved cloud motion vectors. Both channels can sense cloud features during day and night. Compared to 12 μm, the 3.75-μm images exhibit more cloud texture that is very valuable for motion tracking. Figure 3 shows that the correlation curve of image matching between VIIRS and MODIS has a sharper peak at 3.75 μm than at 12 μm, indicating that better motion-tracking precision can be achieved at 3.75 μm. This is because the midwave infrared (MWIR) band provides ~3× better resolution (for diffraction limited systems) compared to LWIR bands. In summary, imaging at 3.75 μm allows for a more compact instrument for the same pixel resolution compared to LWIR, and provides more detailed structure of cloud tops and better determination of cloud motions.

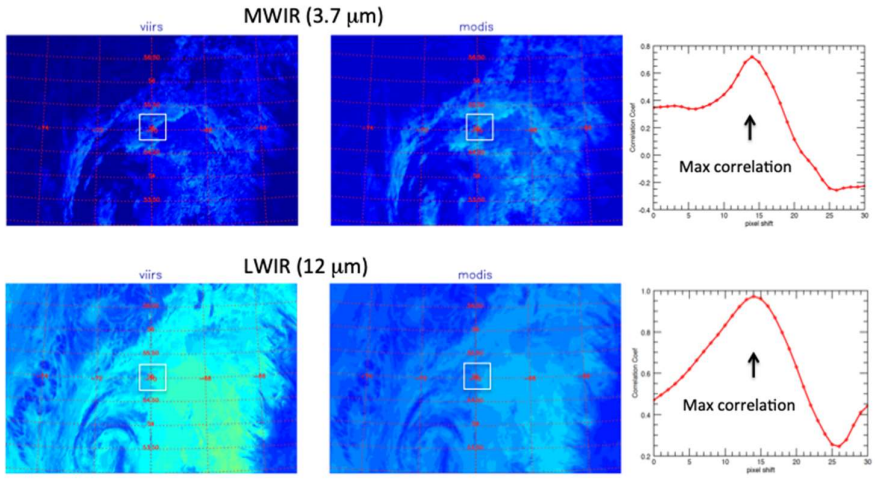

Figure 3. A cloud scene, taken by VIIRS and MODIS near (55°N, 70°W) on April 8, 2016 around UTC 1815 and gridded at 1-km resolution, shows a developing extratropical cyclone that can be readily seen in the 3.75- and 12-μm images. The white box indicates the region for pattern matching between

Preprints (www.preprints.org) | NOT PEER-REVIEWED | Posted: 18 January 2022 doi:10.20944/preprints202201.0262.v1

VIIRS and MODIS, and the pattern matching correlation is showed in the red curve on the right panel. Both 3.7- and 12-μm images produce a shift of 14 pixels between VIIRS and MODIS, which corresponds to ~45 m/s cloud motion as the images were taken ~5 min apart.

Midwave-infrared channels have become a staple of Earth remote sensing with proven capabilities on GOES, POES (AVHRR), JPSS (VIIRS), and Terra/Aqua (MODIS), among others. VIIRS and MODIS use HgCdTe detectors that require cooling down to cryogenic temperatures (80 K). As mentioned above, CMIS employs recently available T2SL technology that has to be cooled only to 150 K. MISR relies on an uncooled CCD which acquires images in the visible and provides a stereo capability like CMIS. Table 1 shows the comparison between measured performance for CMIS and specifications for VIIRS, MODIS, MISR, and ASTER. As described in Table 5 below, the mass of the instrument is 3 kg with average power 8 W (20 W peak power after initial turn on). The overall instrument size is 20 cm × 10 cm × 10 cm for the optical instrument and 9 cm × 9 cm × 9 cm for the electronics. The measured performance of CMIS is competitive with, yet much lower in cost and smaller in size, weight and power (SWaP) than any of these exquisite instruments.

Table 1. Sensor Comparison

	CMIS	**VIIRS***	**MODIS****	**MISR^**	**ASTER^^**
Orbit	415 km ISS orbit	830 km Sun synch	705 km Sun synch	705 km Sun synch	705 km Sun synch
GSD	545 m	375 m 750 m	1000 m	275 m 1000 m	10 m, 30 m, 90 m
Detector	T2SL	HgCdTe	HgCdTe	CCD	CCD/PtSi-S/ HgCdTe
NEdT 3.75 μm at 300 K	0.05 K	0.1 K	0.05 K	N/A	N/A
Optics	Body mounted	Scanning	Scanning	Body mounted	Telescope rotation/ pointing/ scanning mirrors
Cooling	150 K	80 K	80 K	278 K	80 K SWIR and LWIR
Observation	Day/Night	Day/Night	Day/Night	Day	Day/Night

* https://ncc.nesdis.noaa.gov/documents/documentation/viirs-users-guide-tech-report-142a-v1.3.pdf
** https://modis.gsfc.nasa.gov/about/specifications.php
^ https://misr.jpl.nasa.gov/Mission/misrInstrument/
^^ http://asterweb.jpl.nasa.gov

Figure 4 presents an overview of the CMIS instrument design, showing the placement of the ceramic pallet, the filter over the FPA, lens assembly, and cryocooler. The five-zone filter is installed immediately above the FPA (Fig 4b). The system has full frame readout of the FPA with the five regions of interest extracted, one region per filter zone. The only moving parts of CMIS are the cryocooler and calibration mechanism.

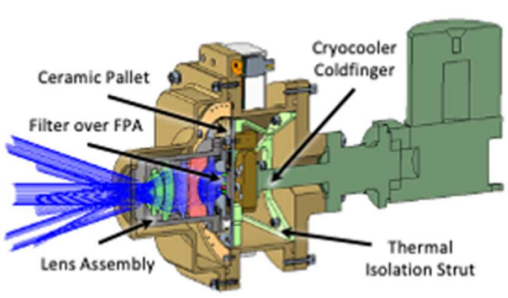

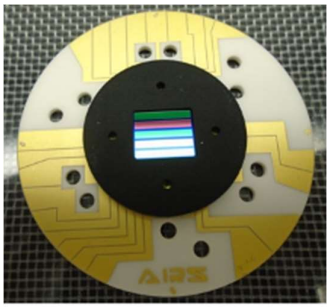

 doi:10.20944/preprints202201.0262.v1

(a) (b)

Figure 4. Depictions of the CMIS instrument. a) Cutout of the CMIS instrument highlighting the locations of the ceramic pallet, filter over the FPA and lens assembly; b) Five zone stripe filter and light shield installed over FPA on the ceramic pallet.

Focal Plane Array (FPA) The FPA has the capability to operate at a frame rate synchronized to the ground advance of one pixel, ~13 Hz for a 415-km orbit. Full 640 × 512-pixel image frames are acquired by the camera electronics which then selects 5 lines for output, one for each filter stripe. There are >32 non-vignetted lines available under each filter that can be processed in the camera electronics. The test flights demonstrated that the calibration for the CMIS detector is very stable with time. Gain coefficients measured more than a year prior yielded brightness temperatures accurate to ±1 K.

The focus of the current paper is to demonstrate multi-angle observations from the 3.75 μm bands for retrieving stereo cloud heights and AMVs. The stereo imaging technique requires only relative intensity measurements from a cloudy scene, as the algorithm tracks and matches the cloud patterns to determine their disparity with respect to the ground. However, calibrated radiances from the CMIS channels will enable additional retrievals of cloud and surface properties, such as temperature and fire intensity. A multispectral analysis of collocated 2.25, 3.75 and 4.05 μm measurements can determine the relative contribution between the reflected solar and thermal blackbody emissions from the atmosphere. A future effort will be devoted to evaluate a solar-corrected brightness temperature at 3.75 μm. During daytime collections, the radiance in the 2.25-μm band will be used to separate the reflected and thermally emitted component of the incident light at 3.75 μm [6]. We can also take advantage of the fact that each temperature has a unique ratio of blackbody radiance at different wavelengths. The ratio of the signals in the 4.05 μm and 3.75 μm bands can thus be used to further refine the temperature measurement. Temperature estimation will be the focus of a future study.

Optics. To meet instrument performance goals, a custom high-speed, wide-field, imaging lens with five elements was developed. A 13-mm focal length provides a 50° by 40° field of view over the detector at a focal ratio of f/1.2. An achromatic design allows the SWIR and MWIR bands to be captured on the same image plane, which enables the lens to be set to a single focus position for both wavelengths.

Cryo System. The pallet holding the FPA, filter and optics is cooled to 150 K, so as to minimize thermal emissions from the lens assembly. Although the outer edge of the lens assembly is exposed to the ambient environment, the cryocooling is expected to reduce stray light, which is crucial to maintain sensitivity at cold temperatures (i.e. T < 240 K). The cryocooler coldfinger is coupled to the pallet by a three-spoke copper strap.

Dewar. CMIS has a vacuum dewar to allow operation of the instrument in an aircraft environment.

Calibration Mechanism. Pixel offset corrections are obtained by periodic views of a thermally-controlled, high-emissivity calibration surface. The CMIS airborne instrument employed a motorized paddle system with a black-painted, large-area thermo-electric (TE) cooler as the calibration surface. The calibration mechanism implements a two-point non-uniformity correction (NUC) at temperatures of 10 °C and 20 °C, which provides sufficient dynamic range to enable accurate measurement of thermal signatures of targets that were considerably colder than the low NUC source. To improve packaging within the CubeSat, a change to a linear mechanism is anticipated for the spaceflight model.

Electronics. CMIS camera electronics (Detector Board, Digital Board and Power Board) were implemented in a small form-factor chosen specifically for CubeSat compatibility. Components were selected and the boards were laid out to accept either low-cost commercial components for the airborne model or their high-reliability equivalents for the spacecraft model.

Preprints (www.preprints.org) | NOT PEER-REVIEWED | Posted: 18 January 2022 doi:10.20944/preprints202201.0262.v1

2.2. Flight Collections

An airborne demonstration of CMIS was conducted in January-February 2021 on the Langley Research Center (LaRC) Gulfstream-III with four round-robin flights out of LaRC. The first flight on 22 January 2021 was an "engineering flight" designed to demonstrate that the airborne instrument setup collected and successfully stored data. The objective of the "engineering flight" was to verify that the flight procedure allowed sufficient time for the instrument to reach its operating temperature of 150 K and that the various instrument commands were executed correctly by the support equipment and software on aircraft. The flight plan for the engineering flight was chosen to cover relatively long, linear ground features to allow the calculation of a high fidelity (pixel-level) lens distortion model. Another objective of this flight was to collect measurements from both cold and warm targets to verify that the instrument meets its designed dynamic range. All objectives of the engineering flight were achieved.

Three science flights were conducted on 27 January, 29 January and 8 February as shown in Figure 5. The case studies and aircraft holds analyzed for this effort are depicted with arrows. The red line segments and boxes show the overpasses of satellites used for validation. Selected cases were limited to periods with stable flight profiles without significant yawing maneuvers or turbulence.

Each flight was designed to collect on cloud features during specific underflights of earth-observing satellites. For example, the purpose of Science Flight #1 was to collect on daytime marine and land stratocumulus and to underfly CALIPSO and MODIS.

(a) (b) (c)

Figure 5: Depictions of the flight paths and analysis regions for (a) Science Flight #1, (b) Science Flight #2, and (c) Science Flight #3. The red boxes and lines denote EOS satellite overpasses within approximately 15 minutes of the CMIS aircraft flight.

As discussed below, the capability to produce AMVs and cloud-top heights (CTHs) for the free troposphere and PBL from CMIS data is demonstrated with these aircraft flights. The flights successfully achieved their primary objectives, which was to show that the sensitivity of the focal plane array and the quality of the images met requirements specified for the instrument (Table 2).

Table 2. Instrument Specification

Criteria	Requirement
Multi-spectral SWIR/MWIR	2.25, 3.75, 4.05 μm
Field of view	≥ 40°
Ground sample distance	≤ 1 km
Distortion	< 10°, software-correctable
Multi-angle	≥ 20°
Sensitivity	NEdT ≤ 1 K at 270 K, 230 K for 3.75, 4.05 μm SNR > 100 for 2.25 μm

Preprints (www.preprints.org) | NOT PEER-REVIEWED | Posted: 18 January 2022 doi:10.20944/preprints202201.0262.v1

Size, Weight and Power	6-U CubeSat compatible

2.3. Geolocation

Conventional imaging generally requires an intricate co-registration process to perform pixel-to-pixel matching for pushframe imagery taken at different rows on an FPA. This procedure is especially critical for images collected from an aircraft due to the continual yawing/pitching motions characteristic of autopilot systems.

Aircraft motions can skew features sometimes by hundreds of pixels, making accurate stereo matching very complicated. To accurately geolocate the airborne CMIS flight imagery, it was necessary to track both the position and orientation of the CMIS pointing relative to an earth-fixed frame. To compensate for aircraft attitude, the flights were conducted with a NovaTel IMU mechanically connected to the rigid plate that carried the CMIS imager. Figure 6 depicts the data collection and processing pipeline for the aircraft flights.

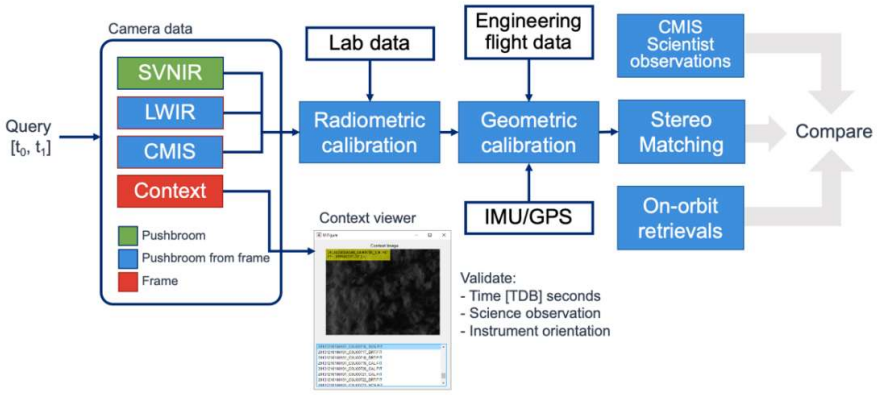

Figure 6. Depiction of the aircraft data collection and processing pipeline.

The initial engineering flight data were used to determine the offset and rotation matrices between the NovaTel IMU and the CMIS sensor, as well as the lens distortion parameters that allow projection of coordinates from the camera image plane to the ITRF93 (earth-fixed) frame. The same rotation matrices were then used for analysis of Science Flights #1 and #2.

Shortly after 2021-02-08 23:00Z, or approximately 90 minutes into the 4-hour Science Flight #3, the NovaTel IMU lost GPS lock and failed to provide a "fine steering" solution. Unfortunately, efforts to correct the problem in-flight were not successful. However, the CMIS imager continued to record data during the NovaTel IMU dropout.

A separate IMU already aboard the NASA Gulfstream III aircraft was available to fill in the missing NovaTel IMU positions and orientations. These auxiliary data came from a logging application, which saved the aircraft's ARINC-429 bus packets, and ran for the duration of the science flight. After much manipulation, the science team was able to incorporate the alternate IMU data stream so that the CMIS imagery acquired during that flight would be scientifically usable.

2.4. Stereo Technique

The CMIS stereo-winds are based on stereo-wind methods successfully applied in several multi-angle, multi-platform cases [4; 7]. Templates are extracted from the CMIS nadir-looking view on a regular grid. Retrieval sites are generally oversampled with respect to the template size, so with an *N*x*M* pixel template and 2:1 oversampling, wind retrieval sites would be arranged in a lattice sampled every (*N*/2)x(*M*/2) pixels. Each

 doi:10.20944/preprints202201.0262.v1

feature template is searched for in both forward- and aft-looking views using a Normalized Cross-Correlation (NCC) algorithm to find matches. Thus, the algorithm does not require absolute radiometric accuracy, but only the relative intensity variations from a feature pattern. The apparent displacement of the feature, or disparity, is interpolated for sub-pixel resolution and tested for significance using the peak NCC value. The fundamental premise of this method is that a translation accurately describes the relationship between the template feature and its match in another view. This premise can be violated when the aircraft experiences turbulence or submits to frequent control inputs during powered flight. To mitigate the adverse impact on feature matching, the imagery is first pre-rectified so that it is uniformly sampled on a plane that is tangent to the WGS-84 ellipsoid at the center of the collect. Along-Track (AT) and Cross-Track (XT) coordinate axes are defined along and across the mean direction of flight. This worked well to improve matching efficiency to yield larger numbers of forward- and aft-nadir matching pairs, but only for cases and holds where the flight trajectory and aircraft attitude were relatively smooth. In other cases, the motion was not sufficiently well compensated in pre-rectification to allow gathering large sets of matches.

There are individual AT and XT components for each of the two fore-nadir and aft-nadir disparities, for a total of four scalar measurements at each retrieval site, from which to estimate a horizontal wind velocity with AT and XT components and a height above the WGS-84 ellipsoid, for a total of three states. The XT component of disparity can be considered mostly due to XT wind velocity as there are typically several tens of seconds in time between acquisitions of the same feature in the forward- or aft-views. The AT component of disparity can be considered mostly due to a combination of geometric parallax and AT wind velocity. It is not possible to separate the geometric height due to parallax and AT wind without either additional observations or a prior assumption about one of them. This is known as the along-track ambiguity. Our retrieval algorithm implements a non-linear least-squares solution to the problem of fitting the best three states (two wind plus height) to the two disparities given the trajectory of the aircraft and the sampling times. A cost to deviate from an *a priori* wind is added to the cost function to be minimized with weightings so that the cost is negligible to deviate XT but prohibitive to deviate AT. This effectively constrains the AT wind to equal the prior value and leaves the height free to fit the data. The result is correct only if the prior value is correct. Alternatively, a prior height can be set and both wind components left free to fit the data. The original intent was to fly two passes over each collection target and combine observations from both passes to jointly estimate AT wind. However, the XT winds tended to carry cloud features out of the narrow swath when revisited, so this approach was largely unsuccessful.

For a single-pass solution, four scalar disparity observations per site with a prior value for either AT wind or height are sufficient to overdetermine the three states, so the residuals after fitting can be used to quantify conformance of the observations to the model. This allows discrimination between good solutions that are properly interpreted as jointly retrieved winds and stereo heights and meaningless ones. We apply a Maximum Absolute Difference (MAD) filter, at a Gaussian-equivalent 3-sigma confidence level, to identify anomalously large residuals in the population of all residuals to discriminate between good (meaningful) and bad (meaningless) solutions with respect to the retrieval model.

3 Results

The objective of the airborne science flights was to assess the performance and capability of CMIS of producing science-quality AMV and cloud height observations under different scenes. The overall flight plan was to collect the data on both clear and cloudy scenes to characterize the sensor's properties.

3.1 Imagery

Preprints (www.preprints.org) | NOT PEER-REVIEWED | Posted: 18 January 2022 doi:10.20944/preprints202201.0262.v1

The scenes presented in this subsection highlight a few examples of the high-quality imagery collected by CMIS. Figure 7 depicts a scene in Florida (Case M) from science flight #2 in which an agricultural field is undergoing a controlled burn. The images show calibrated, geo-referenced radiance for the three CMIS spectral wavelengths. Since the aircraft was not constrained to fly along cardinal direction, the data swath was rotated relative to a standard latitude-longitude Mercator grid. The remaining images will be presented on an AT-XT grid for convenience. The undulations at the boundaries of the image result from the aircraft yaw motion during the autopilot course corrections.

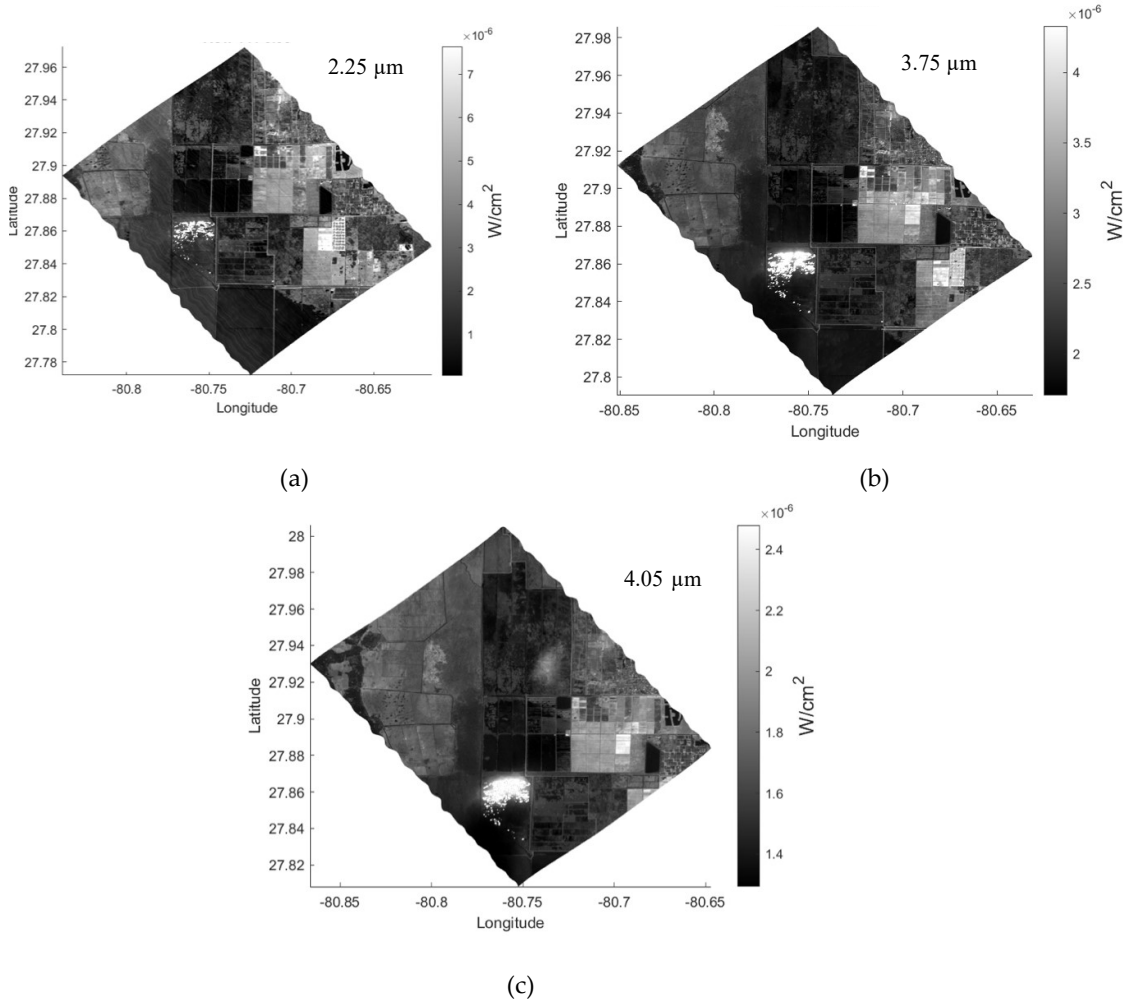

Figure 7. Calibrated, geo-registered irradiance for Case M over Florida during Science Flight #2 on 19 Jan 2021. The figure present images from the (a) 2.25 µm, (b) 3.75 µm (nadir), and (c) 4.05 µm channels, respectively. The direction of flight was toward the southeast.

Some of the radiances from the 3.75- and 4.05-µm bands are saturated in the high temperature regions associated with smoke and gases adjacent to the flames, because of a long integration time used in the data acquisition. Fewer 2.25-µm pixels are saturated because of its narrow bandwidth (50 nm) and blackbody physics.

The different dynamic ranges in CMIS bands can be used collectively for detecting and characterizing fires at a high resolution. It is feasible with the CMIS design to use the 2.25-µm band to make the initial detection and cue the instrument to employ very short integration times for the 4.05-µm band as it passes over the hot spot to avoid saturation. Given the capability of the SWIR channel to detect bright pixels with less saturation and better transmission through smoke and aerosols [8], CMIS can be configured

Preprints (www.preprints.org) | NOT PEER-REVIEWED | Posted: 18 January 2022 doi:10.20944/preprints202201.0262.v1

readily to fly the 2.25-µm and 4.05-µm bands in the fore and aft directions, respectively, for such an agile operation. After collection over the hot spot of interest, the instrument would then return to its nominal integration time for stereo collections at 3.75 µm. Alternatively, the 4.05-µm could be implemented with dual gains.

Figure 8 presents calibrated radiance from the St Lucie Nuclear Power Plant on the east coast of Florida (Case N) on 19 January 2021. With a wider bandwidth and the longer wavelength of the 4.05-µm band, it is more sensitive to temperature variations than the 3.75-µm bands. The temperature differences with one wide warm-water outtake and two cold-water intakes are quite visible at both wavelengths in **Figure 8**. The colder temperatures from the Atlantic Ocean are evident compared to the warmer waters surround the power plant. We also see some evidence of warming in the ocean adjacent to the St Lucie nuclear power plant.

The radiances presented from this daytime scene have an impact of solar contribution. In the MWIR, the radiance from the Earth has roughly equal contributions from the reflected solar radiation and terrestrial thermal emitted radiation. At night, the MWIR bands have sufficient signal to measure terrestrial features. During the day, temperature can be extracted, but requires a method to estimate reflected solar radiance [6].

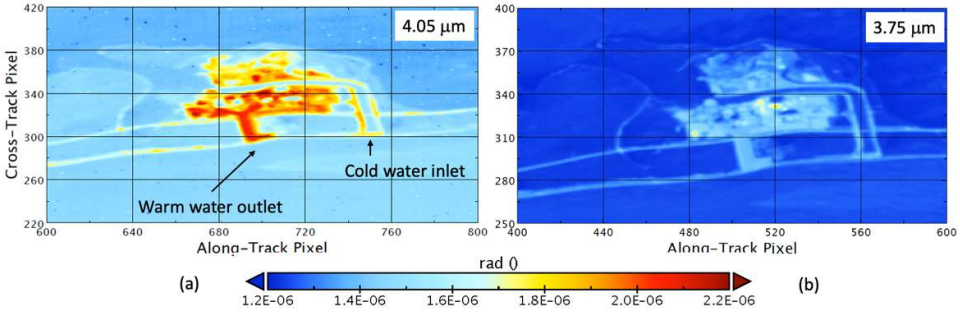

Figure 8. Calibrated radiance for Case N from the St. Lucie Nuclear Power Plant (27.35° N, 80.24° W) on the east coast of Florida during Science Flight #2 on 19 Jan 2021. Radiance from (a) 2.25 µm, (b) 3.75 µm (nadir) are presented. Notice the warm-water outlet and cold-water inlet flowing from and to the nuclear facility, respectively.

3.2 Ground Point Validation

The Hold F flight contains mostly clear-sky land pixels over farmland in the vicinity of Durham, NC during the day. This case offers the opportunity to validate against static targets (i.e., terrain) with known altitudes. The aircraft made two passes over the collection area, but a readout error affected imagery from the first pass (Hold F1), rendering only the second (F2) useable.

The ground sampling for this case is 12.2 m (AT) x 22.8 m (XT) per pixel and the time difference between forward-nadir and aft-nadir looks is a nearly constant ±19 s. Feature templates of 16 x 16 pixels were used to obtain disparity matches at 20373 sites. The retrieval model solved for height and velocity with prior AT velocity set at zero, as it should be for the ground.

Figure 9a features radiance measurements from the 3.75-µm nadir stripe where the aircraft route of flight was from left to right. The radiance across the left 2/3 of the image is fairly uniform due to flat terrain, as indicated by the zero-wind heights shown in Figure 9b. The radiances in the right 1/3 of the image are higher due to the high reflectivity of clouds in the MWIR. Under the assumption of zero along-track winds, the XT winds (Figure 9c) were retrieved with values for this case ranging between -3.0 and 2.4 m/s. The bias-corrected XT winds are very close to zero in the no-cloud region (*i.e.* the terrain is not moving) as they should be. We also note that patterns of what appears to be mass divergence with positive XT winds adjacent to negative XT winds in the cloudy region (Figure 9c). Figure 9d presents the zero-wind heights only for heights below 400 m in order to facilitate comparison with digital elevation map (DEM) heights (Figure 9e**)**. The white area in Figure 9d (*i.e.* no data) is the region obscured by clouds. Comparison

Preprints (www.preprints.org) | NOT PEER-REVIEWED | Posted: 18 January 2022 doi:10.20944/preprints202201.0262.v1

between Figure 9d and Figure 9e shows that the CMIS stereo retrieval replicates the small 50- to 100-m variations in terrain height well.

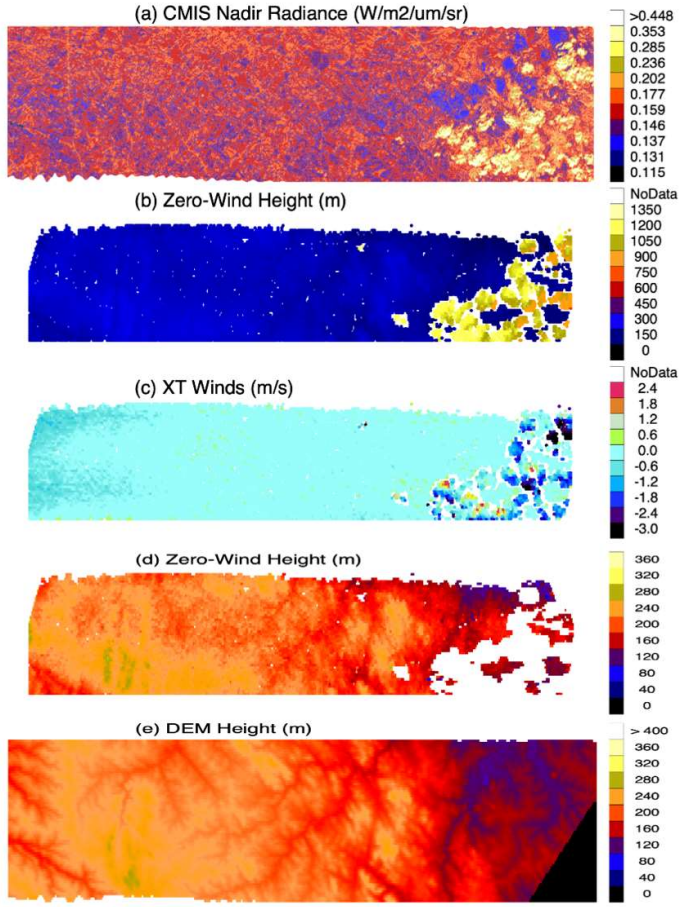

Figure 9. Analysis of hold F2 on 27 Jan 2021 for (a) CMIS calibrated radiance; (b) CMIS zero-wind stereo height; (c) CMIS cross-track winds, (d) zero-wind heights with color contouring to highlight surface elevation differences, and (e) surface height from a digital elevation model (DEM). The direction of flight is from left to right, which is toward the northwest near Durham, NC.

Some systematic error compensation was needed to achieve the best results for this case. Figure 10 shows a 2D-histogram of all retrievals passing the quality criteria. The clouds clearly separate from the clear-sky ground-points, which can be classified by their retrieved height (< 500 m) and speed (< 5 m/s). The ground-point class consists of 16518 sites also meeting the retrieval quality criteria. The retrieved heights of ground points are then compared to the USGS one-arc-second Digital Elevation Model (DEM) and retrieved XT velocity is compared to zero.

Preprints (www.preprints.org) | NOT PEER-REVIEWED | Posted: 18 January 2022 doi:10.20944/preprints202201.0262.v1

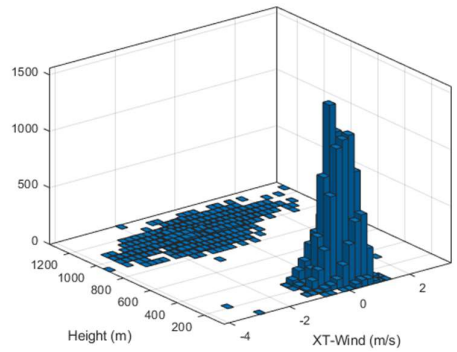

Figure 10. Two-dimensional histogram of retrieved XT wind and height shows low clouds with small XT velocities and a larger population of clear-sky ground retrievals.

Figures 11a, b and c show a point-by-point comparison between the initially retrieved stereo heights and the DEM from Figure 9c. Since the DEM represents height above the geoid, we subtract the geoid height above the WGS-84 ellipsoid equal to -32 m at the center of the collection to represent the terrain height above the ellipsoid. Finally, the DEM is averaged down to assign DEM values at a comparable scale as the templates.

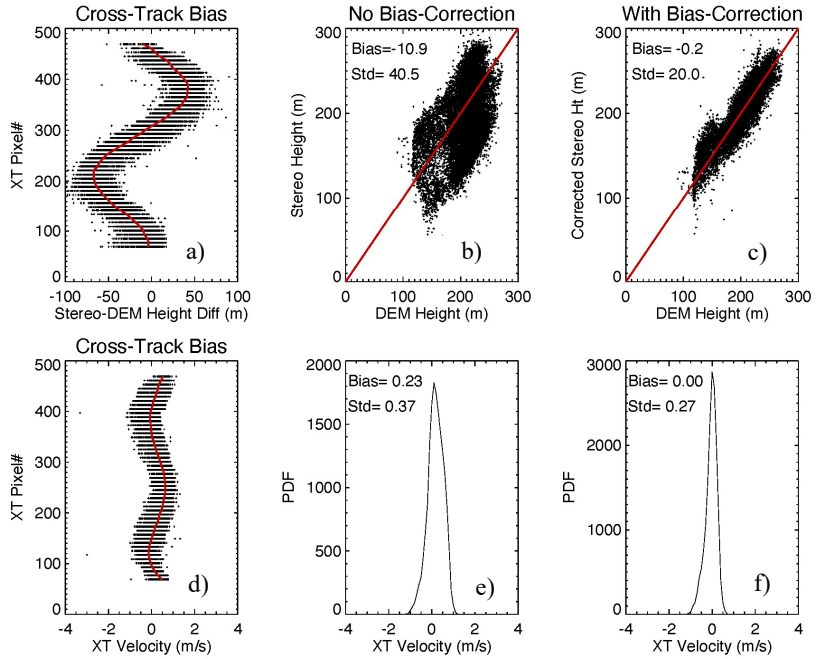

Figure 11. Statistical comparisons for (a) stereo-DEM height difference vs XT pixel; (b) DEM height vs uncorrected stereo height; (c) DEM height vs corrected stereo height; (d) XT velocity vs XT pixel; (e) uncorrected XT velocity vs probability distribution function (PDF); (f) corrected XT velocity vs PDF.

Figure 11 a and d show the cross-track residuals for the initial stereo heights and XT winds, respectively. These are a systematic bias that can be determined empirically as a function of the cross-track pixel number and removed from the initial stereo height and XT wind retrievals. We see in Figure 11 b and e that the biases for the uncorrected CTH and XT winds are ~-11 m and 0.23 m s^{-1}, respectively, which affects their overall accuracy. When the biases are corrected, the standard deviations reduce to 20.0 m and 0.27 m s^{-1} (Figures 11c and f) for the CTH and XT winds, respectively.

Preprints (www.preprints.org) | NOT PEER-REVIEWED | Posted: 18 January 2022 doi:10.20944/preprints202201.0262.v1

The leading hypothesis for the origin of the systematic errors seen is imperfect optical calibration initially done in the laboratory and adjusted in flight using mapped features such as roads. Our analysis of differences between stereo and DEM heights for ground points demonstrates a methodology that can be used in future space flights for geometric calibration or validation.

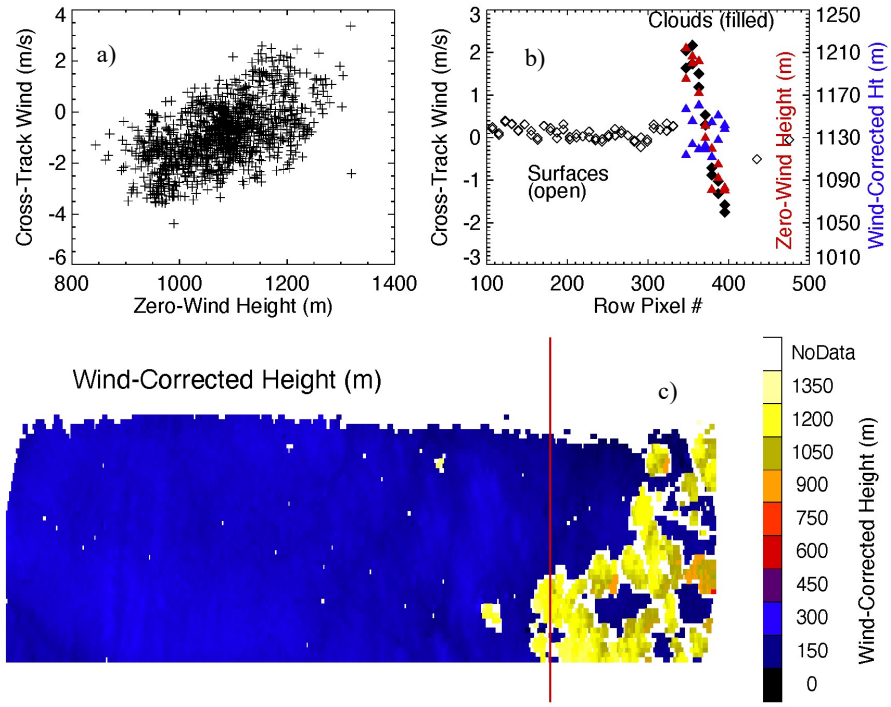

Figure 12. Analysis of Hold F2 for (a) scatter plot of XT wind vs zero-wind height; (b) row pixel # vs XT winds; and (c) wind-corrected height.

A scatterplot of XT wind vs zero-wind height (Figure 12a**)** reveals an apparent correlation between the two fields. When the data are plotted along the transect shown in Figure 12c, an interesting pattern emerges. The XT winds in the cloudy regions are well correlated (Figure 12b) with the zero-wind cloud-top height (CTH; shown in red). As discussed by Mueller et al. [9], if a platform making stereo observations where the AT wind is not negligible, the errors of retrieved zero-wind stereo CTH and unaccounted AT wind are highly correlated. If the CMIS flight maintains a fixed angle with respect to wind direction and the wind direction does not vary, the wind speed variation would result in a significant AT wind component that induces a stereo CTH error. Since the AT and XT winds are correlated under the fixed directional flight, the AT-CTH error correlation manifests itself as the XT-CTH correlation as seen in Figure 12(a,b).

The magnitude for AT winds can be assumed based on the value required to minimize the change in altitude of the cloud-top height. When that was applied for this case (V_{at} = 2.5 m/s), the XT-CTH correlation disappeared, as shown with the blue triangles for the wind-corrected heights and XT winds in Figure 12b**.** The geometry for this situation is illustrated in Figure 13.

Preprints (www.preprints.org) | NOT PEER-REVIEWED | Posted: 18 January 2022 doi:10.20944/preprints202201.0262.v1

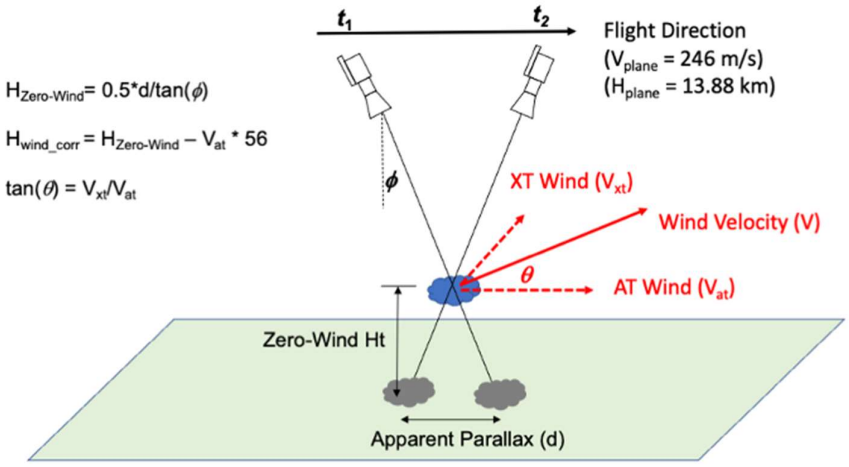

Figure 13. Geometry of stereo calculation to calculate wind-corrected height. The factor 56 (m per m/s) is the time elapsed between observations.

3.2 CALIPSO Under-Flight

The Hold D flight path covers a nearly homogenous cloud field above Western Pennsylvania nearly simultaneously with an overpass by CALIPSO approximately at 19:00Z on 27 January 2021. For this case, we constrain the wind height using CALIPSO and solve for both wind vector components. This case provides a good example of the synergy between simultaneous aerosol-cloud LiDAR and stereo observations. Figure 14 shows the CMIS retrieval sites for Hold D1 with collocated CALIPSO vertical profiles.

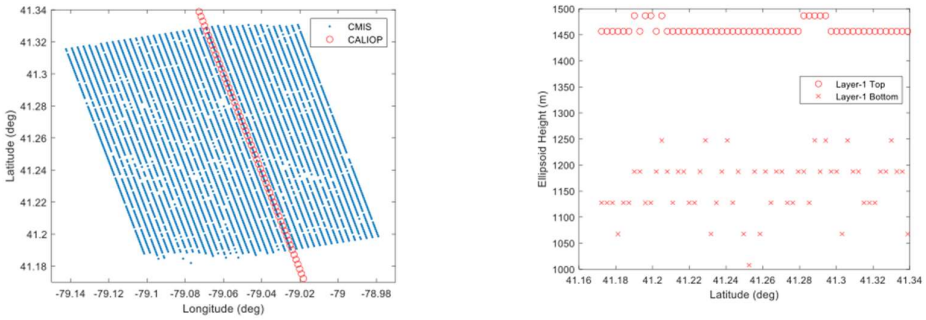

(a) Collocated Retrievals (b) CALIOP Layer-1 Heights

Figure 14. (a) CMIS retrieval sites for Hold D1 are collocated in space and time with those of CALIOP and (b) CALIOP layer-1 cloud tops and bottoms show nearly constant cloud-top heights in the curtain over the collect. CALIOP heights from the 333-m cloud-layer product have been referenced to the WGS-84 ellipsoid by adding the geoid height of -33 m at the center of the collect.

Typically, CALIOP detects clouds and aerosols at lower optical depths than passive imaging, and so CALIOP heights may be higher than those detected with stereo methods [10]. Fixing the mean height for the CMIS wind field at 1400 m, we retrieve CMIS AT and XT winds over the collect with distributions as shown in Figure 15. These are rotated into U (+East) and V (+North) vector components to show mean wind vector values of (3.38, -4.39) m/s.

Preprints (www.preprints.org) | NOT PEER-REVIEWED | Posted: 18 January 2022 doi:10.20944/preprints202201.0262.v1

(a) AT-XT Winds and Height

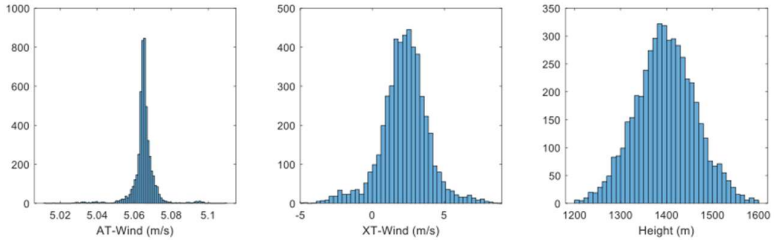

(b) U-V Winds and Height

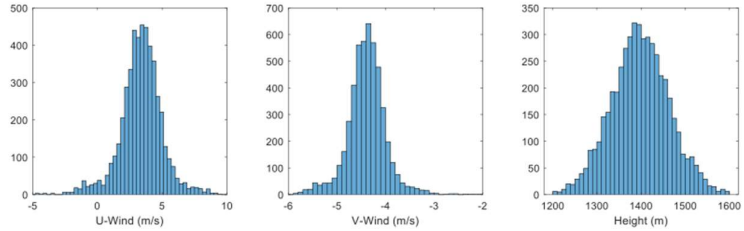

Figure 15: CMIS winds over Hold D1 where the mean wind height is constrained to approximate the CALIOP layer-1 top are shown with (a) winds resolved AT-XT and (b) U-V.

The Hold-D1 collection has an Aqua overpass approximately an hour earlier at 17:55Z that was used for MODIS and GOES-16 stereo winds to corroborate the CMIS results. A larger domain (41.25±1°, -79.05±1°) is considered since the density of satellite retrievals is much less than those from CMIS and there is approximately a one-hour time mismatch. The distribution of MODIS-GOES stereo winds within this domain is shown in Figure 16. The mean CMIS retrieval of (3.38, -4.39) m/s falls near the most probable satellite U-V winds and its 5.54 m/s speed and mean height of 1400 m also falls near the most probable speed-height combinations.

(a) U-V Wind Distribution (b) Speed-Height Distribution

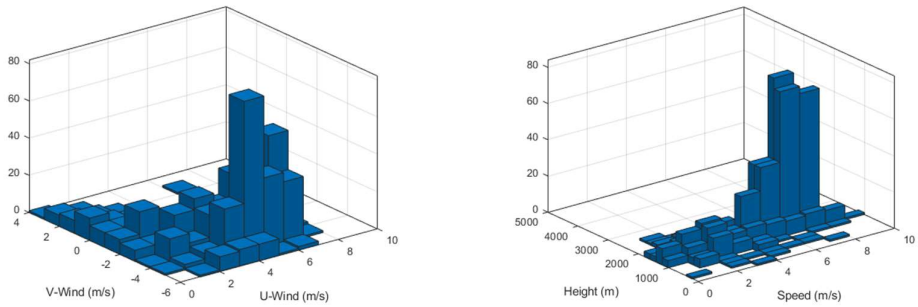

Figure 16: (a) Joint distribution of U-V winds and (b) speed-height from the MODIS-GOES stereo run corroborate the CMIS winds.

3.2 Aeolus Under-Flight

The Hold J flight was designed to fly along the track of Aeolus on 8 February 2021 at night. It is also within the coverage of both GOES-16 and -17. We use the stereo winds from GOES-16 and -17 [7] to set the *a priori* value of the AT wind for the CMIS retrievals and compare against Aeolus. The first pass (J1) was the most simultaneous to the Aeolus Mie wind retrievals. CMIS was 5 minutes ahead of Aeolus over Hold J, which was

Preprints (www.preprints.org) | NOT PEER-REVIEWED | Posted: 18 January 2022 doi:10.20944/preprints202201.0262.v1

completely cloud covered. Sites for the three sets of retrievals are shown in Figure 17. The sampling scales are quite different, with CMIS densely sampling over a very small patch due to the low altitude of the aircraft (compared to satellites). The GOES stereo winds used a triplet of CONUS scenes centered on 23:36Z from GOES-16 and a doublet of contemporaneous Full Disk scenes from GOES-17. The GOES stereo winds in the neighborhood reveal a cloud layer at 4813 m median height and with median winds resolved along and across the direction of the CMIS flight of 2.76 m/s (AT) and -35.07 m/s (XT). We use 2.76 m/s for the prior value of the AT wind in the CMIS retrieval code and solve for XT wind and CTH at each CMIS retrieval site.

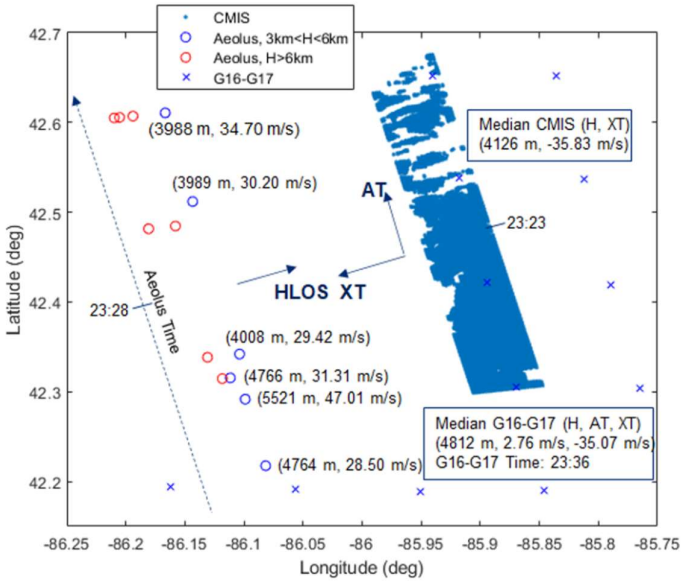

Figure 17. Retrieval sites for Aeolus, GOES stereo, and CMIS wind retrievals are indicated, showing a vast difference in sampling densities between the aircraft and satellite observations.

Figure 18 compares AMVs and CTHs from GOES and CMIS against Aeolus Mie winds. There is broad agreement for all three estimates, although Aeolus wind retrievals are biased about 5 ms^{-1} lower than those retrieved using GOES and CMIS. The XT winds for CMIS match fairly well with G16-G17 stereo winds. We see a local minimum (in magnitude) for both GOES and CMIS near 42.6° N. A similar local minimum appears for Aeolus near 42.7° N. The height retrievals for CMIS (Figure 18b) match the overall shape of those for G16-G17 stereo. We see decreasing CTH between 42.3° and 42.5° for both GOES and CMIS, although the decrease is steeper for CMIS. This may be due to the very fine GSD for the CMIS aircraft payload. CMIS demonstrated good sensitivity to small-scale variability.

Preprints (www.preprints.org) | NOT PEER-REVIEWED | Posted: 18 January 2022 doi:10.20944/preprints202201.0262.v1

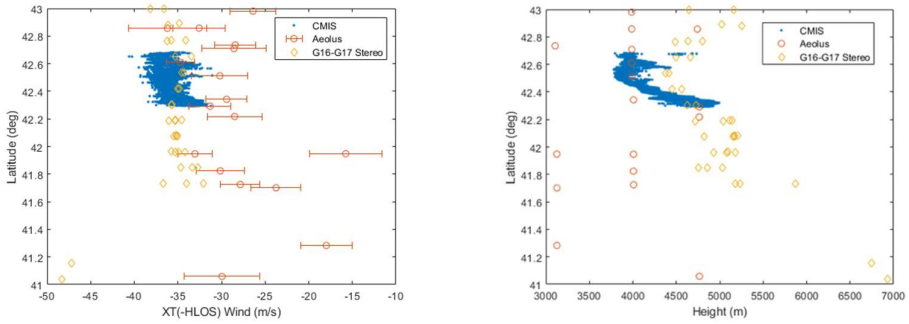

(a) (b)

Figure 18. Comparison between Aeolus, G16-G17 stereo, and CMIS stereo for (a) cross-track winds and (b) stereo heights over Wisconsin on 8 Feb 2021.

The retrieval histograms are shown in Figure 19. The XT wind distribution is quite narrow, and its median value of -35.83 m/s is a good match with the median GOES stereo wind of -35.07 m/s (XT). The distribution of CMIS heights is broader, but the GOES stereo-wind median is in the range toward the upper end.

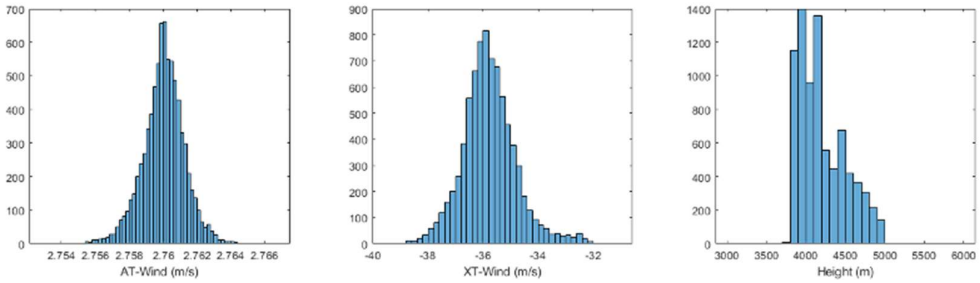

Figure 19: Histograms show the wind retrievals passing the quality criteria. The AT winds are very close to the prior value used.

There are six Aeolus Mie winds in the relevant atmospheric layer. Because the flight line was nearly parallel to the Aeolus track, Aeolus Horizontal to Line of Sight (HLOS) wind components are opposite in direction to the XT winds from CMIS. Aeolus and CMIS winds are similar but not as well matched as the GOES stereo winds. None of the datasets compared are perfectly aligned in time, location, or scale.

4. Discussion

The CMIS instrument provides three angular views at 3.75 μm, wide-swath coverage and day-night sensing compatible with a compact 6U-CubeSat design to enable global coverage of the winds and cloud heights in the free troposphere and PBL. Stereo sensing at a wavelength of 3.75 μm permits 24/7 day/night sensing to observe diurnal variation of PBL structures. However, when the clouds are moving in the direction of the spacecraft velocity vector, the stereo technique applied to a single LEO satellite suffers from an aliasing problem in which errors in along-track wind and CTH are highly correlated as is known from MISR [9] and discussed here. To resolve this ambiguity, stereo imaging requires independent observations from multiple platforms (*i.e.* joint retrievals). This joint technique can be applied to LEO-LEO platforms or LEO-GEO platforms. It would also be most relevant for a series of CubeSats in a leader-follower configuration (*i.e.* pearls on a string).

Preprints (www.preprints.org) | NOT PEER-REVIEWED | Posted: 18 January 2022 doi:10.20944/preprints202201.0262.v1

The stereo methodology applied to LEO-LEO satellites is particularly valuable for the polar regions where detection of low-level clouds and semi-transparent clouds is a major challenge for satellite remote sensing. The most accurate method for retrievals at high latitudes could potentially be leader-follower satellites if favorable viewing geometries and optimized spacecraft separation times are maintained. The airborne flights presented here described the sensitivity to detect patterns in PBL clouds during day/night was sufficient to perform stereo retrievals. Due to frequent turbulence and course corrections, retrievals from an aircraft are much more difficult to do accurately than from space. The following section describes how CMIS can be accommodated on a CubeSat or as a hosted payload with appropriate capabilities for attitude and pointing knowledge.

4.1 Implications for Notional Spaceflight

The following subsection presents a simple analysis to estimate the accuracy of the retrievals for a spaceflight. These results are then be used to specify general requirements for a CubeSat to host a stereo wind sensing mission.

Accuracy

Some very simple geometric relationships can help us estimate stereo wind retrieval accuracies and scale them from an airplane to a spacecraft (our retrieval software using a full fidelity and nonlinear model). Such estimates can be confirmed from the retrieval process, which outputs the three retrieval states (two horizontal wind vector components and the height) along with their 3x3 covariance matrix. The latter can be interpreted as representing the uncertainties in the states with modeled errors in the input disparities. Figure 20 shows an idealized configuration with a single CMIS flying over the locally flat Earth surface (or a tangent plane to the WGS-84 ellipsoid). We assume that CMIS flies at a constant altitude H and ground speed V along the x axis. The three stereo line arrays are perpendicular to the direction of motion and parallel to the y axis (into the paper). Consider only those points directly under the flight track ($y = 0$). A cloud feature seen by each line array is assigned apparent geographic coordinates (x_n, y_n) in each of the three looks ($n =$ forward, nadir, aft) at acquisition times t_n. The angle α is fixed by the CMIS camera design.

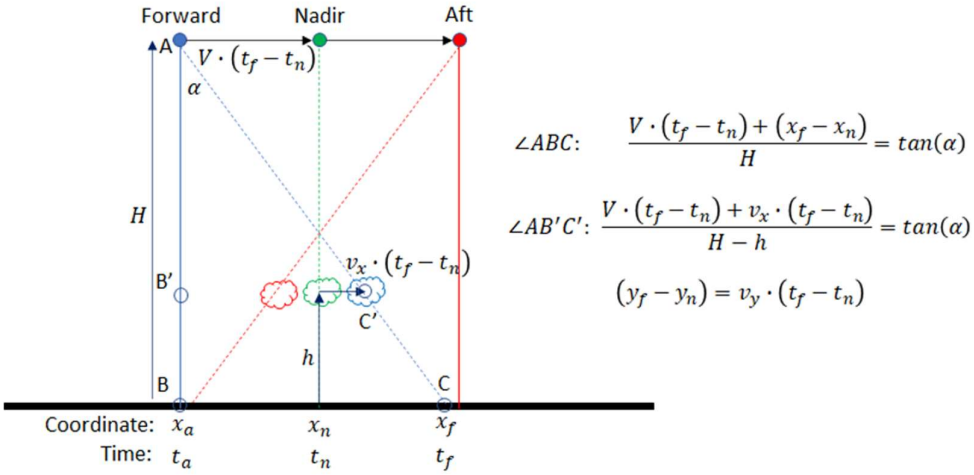

Figure 20. Simplified CMIS configuration allows linear design rules to be derived using elementary geometry. Non-simultaneous forward, nadir, and aft looks are shown for a single camera. Forward and aft coordinates for a cloud feature seen in the nadir look are given at the matched locations in the forward- and aft-looks.

$\angle AB'C'$ as shown in Figure 19 allows for the solution for the acquisition time difference, which is substituted into the tangent formula for $\angle ABC$. In a spacecraft

 doi:10.20944/preprints202201.0262.v1

application, the wind speed and height are typically much less than the ground speed and altitude of the spacecraft (i.e., $h \ll H$ and $v_x \ll V$), which leads to an approximately linear relationship between the states:

$$\left(x_f - x_n\right) = v_x \cdot \frac{H}{V} tan(\alpha) + h \cdot tan(\alpha). \quad (1)$$

A nearly identical formula applies to the aft-nadir combination. Since it has the same coefficients as Equation (1), the height h and along-track velocity v_x cannot be decoupled and an assumption must be made about one of these states; however, using the aft-nadir combination does reduce the uncertainty in the retrieval. If the along-track velocity is assumed zero ("zero wind" retrieval) when it is not, we can see that this will bias the retrieved height by

$$\Delta h = \frac{H}{V} v_x. \quad (2)$$

The cross-track wind v_y can be similarly written as a linear function of only the cross-track coordinate difference by eliminating the time difference in the same manner:

$$\left(y_f - y_n\right) = v_y \cdot \frac{H}{V} tan(\alpha). \quad (3)$$

A second acquisition of the tracked feature from another platform will provide the additional information to allow the decoupling of h and v_x. This could be an acquisition from a geostationary (GEO) satellite or another low-Earth orbiter (LEO). The GEO-LEO combination has been extensively discussed in Carr et al. [4] and demonstrated with MISR and GOES-R to achieve better than 200 m height and 0.5 m/s retrieval accuracies. It offers the advantage of allowing the effective transfer of Image Navigation and Registration (INR) – or geolocation – knowledge from the presumably high accuracy GEO to the more modest accuracy LEO using a "bundle adjustment". The bundle adjustment is possible because of the overdetermination of the dual-satellite retrievals.

Of particular interest for this paper is the case where a second CMIS follows the first. Matches would be made from the nadir look of the leading satellite into up to five other looks (leader-forward, leader-aft, follower-forward, follower-nadir, and follower-aft). This configuration enables a constellation of CMIS sensors to cover areas without GEO coverage, including the poles, for a full global capability. Supposing that the leader-follower time separation is T, we consider the nadir looks as shown in Figure 21. The acquisition time difference can be solved for using the spacecraft (S/C) equation to eliminate it in the other, and after linearizing in the variable v_x and similarly for v_y:

$$(x_{n2} - x_{n1}) = v_x \cdot T. \quad (4a)$$

$$(y_{n2} - y_{n1}) = v_y \cdot T. \quad (4b)$$

Preprints (www.preprints.org) | NOT PEER-REVIEWED | Posted: 18 January 2022 doi:10.20944/preprints202201.0262.v1

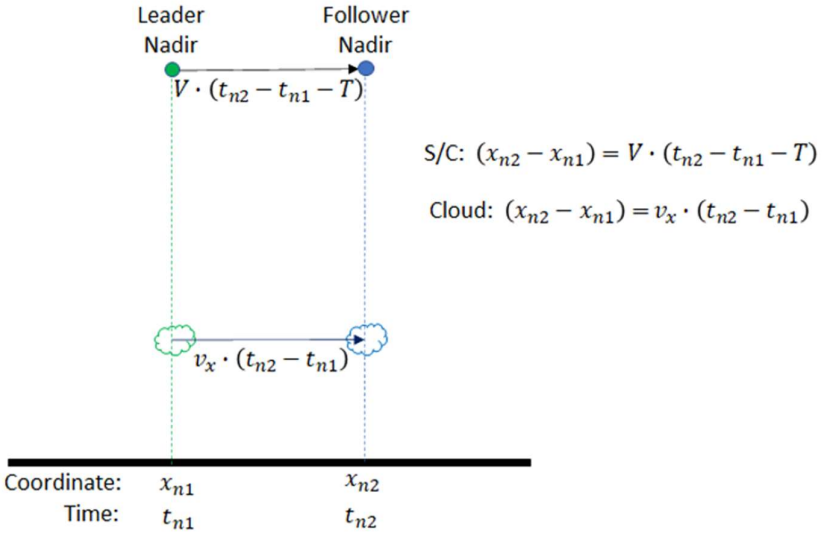

Figure 21. Leader-follower matches enable unambiguous determination of the along-track winds. Consecutive nadir acquisitions are shown, which is the simplest case.

Equations (1), (3), and (4) can be used to calculate, for example, $(x_{f2} - x_{n1}) = (x_{f2} - x_{n2}) + (x_{n2} - x_{n1})$. The full systems of equations for the states (h, v_x) and v_y are therefore:

$$\begin{bmatrix} x_{f1} - x_{n1} \\ x_{a1} - x_{n1} \\ x_{f2} - x_{n1} \\ x_{a2} - x_{n1} \\ x_{n2} - x_{n1} \end{bmatrix} = \begin{bmatrix} tan(\alpha) & (H/V)tan(\alpha) \\ -tan(\alpha) & -(H/V)tan(\alpha) \\ tan(\alpha) & T + (H/V)tan(\alpha) \\ -tan(\alpha) & T - (H/V)tan(\alpha) \\ 0 & T \end{bmatrix} \begin{bmatrix} h \\ v_x \end{bmatrix}, \tag{5a}$$

$$\begin{bmatrix} y_{f1} - y_{n1} \\ y_{a1} - y_{n1} \\ y_{f2} - y_{n1} \\ y_{a2} - y_{n1} \\ y_{n2} - y_{n1} \end{bmatrix} = \begin{bmatrix} (H/V)tan(\alpha) \\ -(H/V)tan(\alpha) \\ T + (H/V)tan(\alpha) \\ T - (H/V)tan(\alpha) \\ T \end{bmatrix} [v_y]. \tag{5b}$$

We can now estimate retrieval accuracy considering the geolocation accuracy expected from a low-cost CubeSat system flying at an International Space Station (ISS) altitude $H = 410$ km with $V = 7.7$ km/s. We will also assume $\alpha = 20°$ and a cross-track field of view of ±25°, which is similar to the optical configuration of the air campaign. Using GPS allows for very accurate positioning of the spacecraft (~4 m) and time tagging of observations; therefore, attitude knowledge and calibration of the optics are likely the drivers in terms of geolocation accuracy. A pixel count of 1280 provides for a ground footprint of 150 m. At this resolution, pointing knowledge of 0.005° that is obtainable in a CubeSat translates to ~40 m on the ground, which is about a quarter of a pixel. Matching also suffers from some uncertainty, which from our experience with GEO-LEO and GEO-GEO stereo winds can be expected to be ~0.5 pixels. Therefore, a good design goal for the uncertainties in each Δx and Δy would be $\sigma = \sqrt{2 \cdot 0.25^2 + 0.5^2} \sim 0.6$ pixel (i.e., 100 m). Equations (5) are overdetermined, so they should be solved by least-squares. Designating the coefficient matrices in Equations (5) as M_x and M_y, and assuming the uncertainties in each Δx and Δy are independent from each other enables an estimate of the retrieval accuracy. The covariances for the states are:

$$cov(h, v_x) = \sigma^2 (M_x^T M_x)^{-1}, \tag{6a}$$

$$cov(v_y) = \sigma^2 (M_y^T M_y)^{-1}. \tag{6a}$$

Preprints (www.preprints.org) | NOT PEER-REVIEWED | Posted: 18 January 2022 doi:10.20944/preprints202201.0262.v1

Since the time T between leader and follower has not been specified, we vary that parametrically. Figure 22 plots the retrieval uncertainties (square-roots of the diagonal elements of the covariances) using this model as a function of T.

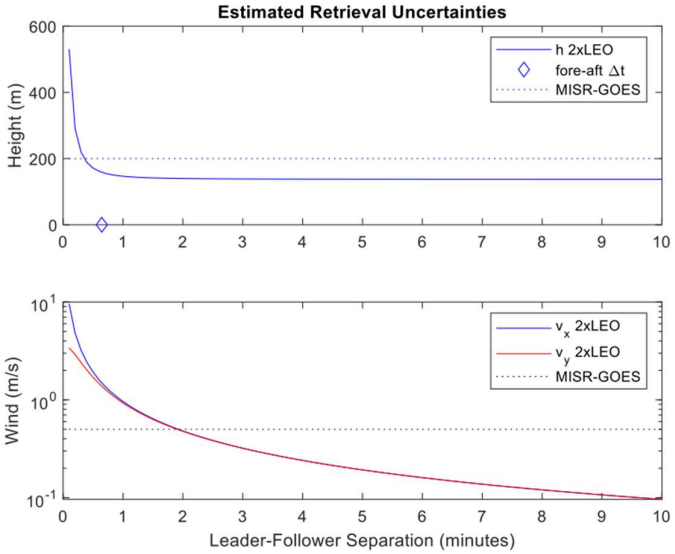

Figure 22. Leader-Follower retrieval uncertainties as a function of separation between the satellites. The simplified model includes only random errors. The practical accuracies achieved using the MISR A cameras and GOES are shown as dashed lines independent of the time separation between MISR and GOES acquisitions [4]. In practice, the contributing errors are more nuanced and include, for example, the effect of cloud shape changes that grow with T. Good results with operational satellites winds are achieved with $T = 1$, 5, and 10 minutes that are characteristic of GOES-R MESO, CONUS, and Full Disk repetition rates. As Tgrows to 15 minutes and beyond, cloud shape changes begin to affect matching accuracy and diminish the number of high-quality matches.

This solution assumes no cloud deformation with time. For certain cloud types such as small cumulus, the overall lifetime could be less than 10 minutes, so the reduction in uncertainly for winds may not always obtain for such cases.

For sngle-camera zero-wind retrievals, Equation (2) provides the systematic error, and the random error is estimated by coefficient matrices in the reduced system of equations:

$$\begin{bmatrix} x_f - x_n \\ x_a - x_n \end{bmatrix} = \begin{bmatrix} tan(\alpha) \\ -tan(\alpha) \end{bmatrix} [h], \tag{7a}$$

$$\begin{bmatrix} y_f - y_n \\ y_a - y_n \end{bmatrix} = \begin{bmatrix} (H/V)tan(\alpha) \\ -(H/V)tan(\alpha) \end{bmatrix} [v_y]. \tag{7b}$$

The uncertainties in the retrieved zero-wind states (h, v_y) are therefore,

$$\sigma_{h(v_x=0)} = \frac{\sigma}{\sqrt{2}tan(\alpha)}, \tag{8a}$$

$$\sigma_{v_y} = \frac{V}{H}\frac{\sigma}{\sqrt{2}tan(\alpha)}. \tag{8a}$$

The asymptotic value for σ_h in Figure 22 turns out to be equal to $\sigma_{h(v_x=0)}/\sqrt{2}$; therefore, the look-ahead/behind angle α governs the height retrieval uncertainty in both the zero-wind and leader-follower configurations.

Preprints (www.preprints.org) | NOT PEER-REVIEWED | Posted: 18 January 2022 doi:10.20944/preprints202201.0262.v1

Relating to the aircraft collections, consider Hold F2, where H~13.85 km, V~245 m/s, $\alpha = 19°$, and the ground-sampling distance is ~12.2 m along-track and ~22.8 m cross-track. The residual standard error from Figure 11 in the ground retrievals for Hold F2 was 20.2 m, implying a residual geolocation error of 9.8 m along-track or 0.8 sampling distances. The residual standard wind velocity error in the Hold F2 ground retrievals was 0.27 m/s, implying a residual geolocation error of 7.4 m cross-track or 0.3 sampling distances. These implied geolocation errors are in family with the geolocation errors in pixels assumed for a spacecraft.

If the standard geolocation error were 10 m in each axis in the aircraft flights, then the covariance matrix from the retrieval process would provide an estimate of the standard errors for the retrieved states that can be compared with Equations (8). This comparison is provided in Table 3 to confirm that the simplified model provides a good estimate of retrieval accuracy and therefore is useful for mission design purposes.

Table 3. Comparison between the simple model of Equations (8) and uncertainties derived from the retrieval covariance matrix shows good agreement. A 10 m geolocation error was assumed everywhere within the Hold F2 collection. The covariance model results have a very small dependence on cross-track position and height above the ellipsoid.

	σ_{v_y}	$\sigma_{h(v_x=0)}$
Equations (8)	0.36 m/s	20.5 m
Covariance Model (mean)	0.37 m/s	20.7 m

Accommodation

Table 4 shows pertinent parameters for CMIS flown at different altitudes. The swath width is calculated from the cross-track field of view and number of cross-track pixels. For a nominal altitude of 800 km, the swath width and ground sample distance at nadir are 757 km and 1091 m, respectively, for detector format 640 x 512 pixels. However, with recent developments in detector technology, we expect to upgrade the detector format used for the spaceflight version of CMIS to 1280 x 1024 pixels, which would reduce the GSD to about 545 m for an 800-km orbit and 275 m for a 410-km orbit.

Table 4. Performance parameters for CMIS flown at different orbital altitudes

Altitude (km)	100	400	550	800	915	1130
Cross-track FOV (°)	50	50	50	50	50	50
Cross-track pixels	640	640	640	640	640	640
Swath width (km)	93	376	518	757	868	1076
GSD nadir (m)	136	545	750	1091	1248	1541
GSD edge (m)	167	678	940	1386	1596	1997
Measurement Spacing (s)	9.3	40.4	57.5	88.6	103.9	134.4

Table 5 shows the requirements for the spacecraft to accommodate CMIS. The size and power requirements derive from the airborne unit flown on the Gulfstream III. The position/attitude requirements derive from the uncertainty analysis presented above. For two spacecraft in leader-follower formation at an altitude of 410 km, our analysis suggests that a pointing accuracy of ±0.005° should provide uncertainty to within 180 m and 0.5 m/s respectively for the cloud top and wind velocity, respectively. A pointing stability of 36 arc-sec/ 1-sec should enable sufficient steadiness to achieve reasonable pattern matching.

Table 5. Spacecraft Accommodation

	Parameter	**Requirement**
	Mass	3 kg

Payload Accommodation	Size	Optical Unit: 20 × 10 × 10 cm Electronics: 9 × 9 × 9 cm
	Power	20 W peak for initial cool-down 8 W average
Position/Attitude	Position knowledge	4 m
	Pointing Accuracy	±0.005°
	Pointing Stability	36 arc-sec/ 1-sec
Data	Data Transfer Rate	600 kbps
	Data Storage	10.4 GBits
	Data Downlink	5.2 Gbits/day

As discussed above, attitude control and knowledge for CubeSats are now sufficient to produce high-quality stereo products. The primary issue remains data return due to available power on a CubeSat. The most likely method of communications would be via an S-band transceiver, which results in practical limits on the amount of data that can be downlinked during a given pass. One approach for this limitation is to increase the number of ground stations that the data can be downlinked. However, this can rapidly drive up costs and defeats the purpose of employing a low-cost constellation. A better approach might be to use onboard processing to calculate the disparities between the three 3.75-μm stripes on each satellite, which would significantly reduce the volume of data to be downlinked. Thus, onboard processing applied judiciously could be used to enable the system to collect data 24/7 [11].

4.2 Complement to active 3D winds

Lidar-derived winds from Aeolus presented in Figure 18 show that the swath width from an active system is very narrow compared to an EO/IR passive system. The advantage of lidar is that it has the potential to retrieve winds over clear and cloudy regions, while CMIS is limited to cloudy regions (at present). The horizontal resolution for Aeolus data is approximately 90 km for Rayleigh clear-sky winds and 10 km for Mie cloudy sky winds [12]. CMIS could effectively complement Lidar observations by providing higher horizontal and vertical resolution datasets over wider swaths. The GSD as a function of orbit altitude is shown in Table 3 above.

4.3 Planetary Boundary Layer

Previous studies have identified the PBL height (PBLH) as a key length parameter for modeling cloud/aerosol entrainment, vertical diffusion, turbulence mixing, convective transport, and atmospheric pollutant deposition [13-16]. As a satellite observable, CTH serves as a critical observational constraint to PBLH. In the case of marine boundary layer, stratocumulus clouds are capped by strong temperature inversion at the top of PBL. Therefore, the MBL CTH is a good measure of PBLH [*e.g.* 17-19]. CTH has also been used to infer the PBLH of stratocumulus-topped continental [20] and Arctic [21] boundary layers.

It has been a great challenge for spaceborne sounding to accurately resolve the PBLH because it is often too close to the surface. Current observations of PBL depth from radiosondes remain sparse and a global dataset of PBL depth and its variations is needed.

Karlsson et al. [22] showed that the stereo CTH from Terra/MISR is able to capture the PBLH variation in a stratocumulus-to-trade-cumulus transition off the coast of California. PBL cloud observations from MISR also helped to better characterize Arctic clouds and their radiative impacts [23; 24]. Thus, a multi-angle and multi-platform (MAMP) stereo method was developed to overcome the correlated-error problem and successfully implemented for the MISR-GEO pairing [4]. A pairing between MODIS and GEO satellites was also developed to extend the coverage to both day and night with a wider swath [25]. However, Carr et al. [25] also showed that the MODIS-GEO pairing suffers from stereo blind spots where the look angles for both platforms are parallel. Stereo blind spots would also occur in a VIIRS-GEO pairing. In contrast, CMIS provides a single integrated instrument that is well-suited to all of these pairings and without stereo blind spots.

5. Conclusions

The results presented in this paper from the CMIS aircraft flights demonstrated the advanced capability of the instrument for multi-angle, multi-spectral wide-field of view observations to support earth science. The accuracy of the airborne stereo observations of cloud heights and winds confirmed that this MWIR technique applied to CMIS datasets can be used for spaceflight.

The CMIS observations with MWIR bands demonstrated that the instrument delivers scientifically-useful day/night stereo observations for AMVs and their heights. The MWIR imaging has an advantage over the thermal bands in the dimension of instrument optics for the same pixel resolution, which allows the compact design of CMIS. Although the MWIR bands have been flown on LEO and GEO, the key enabling technology is the high-sensitivity Type-2 Superlattice (T2SL) detector used by CMIS that operates at 150 K. The high detector operation temperature will significantly lower the instrument power, prolong the cooler lifetime, and simplify the system design.

The CMIS aircraft flights proved that its technology and design are ready for spaceflight. The current detector format for CMIS is 640 x 512 pixels with a 50-degree field of view. At a nominal altitude of 550 km, the GSD is approximately 750 m as indicated in Table 2. However, the technology has improved so that the detector can now be scaled up to 1280x1024 pixels, which would improve the GSD to 375 m. This provides sufficient horizontal resolution to observe mesoscale features associated with such features as outflow boundaries and PBL structures.

The low SWaP (size, weight, and power) of CMIS makes it a cost-effective solution to the need for high-resolution spatiotemporal sampling from CubeSat or SmallSat constellations. Its compact design will fit the instrument to a 6U CubeSat or as a hosted payload on a SmallSat, to meet the Earth Science 2017-2027 needs for high-resolution tropospheric and PBL winds. With the improved SWaP, CMIS provides an attractive, affordable option to fly a satellite constellation of 10-15 satellites for a potential Earth System Explorer mission to meet requirements for the Atmospheric Winds Targeted Observable (TO-4 in Appendix C of ESAS 2017) or a potential Earth Venture science mission. If the objective is to obtain stereo cloud motion vectors only, highly accurate radiometric calibration would not be required. A calibration need only be accurate enough to enable pattern matching between cloud scenes taken within 10-15 minutes of each other.

As demonstrated from the CMIS airborne flights, the instrument also proved its capability for monitoring fires. The 4.05-μm band provides data in combination with the 2.25-μm band to estimate temperature and fire radiative power if both bands remain unsaturated. The CMIS instrument can utilize dual gains to achieve a wider dynamic range so as to avoid saturation. Depending on wildfire measurement requirements, the instrument can be upgraded to increase the number of spectral channels to ~10 within the range of 1.8 μm to 5 μm. Accurate radiometric calibration, plus a large dynamic range would be required to enable sensing of large, hot fires, as well as volcanic plumes.

For a potential future mission, it might also be advisable to include a 2048-pixel visible band with time-delay integration to serve as a low-light imager. On moonlit nights, it might be possible to obtain stereo products at better than 250-m and 375-m GSD with a low-light imager and CMIS, respectively. The high data rates for these imagers would drive the need for on-board processing to process the datasets into disparities, which are an intermediate-level stereo product. The stereo-bit FPGA has already demonstrated the capability to do this [11].

Finally, because of the high operating temperature of the FPA, a potential design enhancement for CMIS would be to replace its cryocooler with a TE cooler. The cryocooler used by CMIS has significant flight heritage, but it introduces vibrations as well as a limited lifetime. The current state of the art for TE coolers is an operating temperature of about 180 K, which is about 30 degrees warmer than that needed by CMIS. TE coolers have the advantage of no moving parts, plus no significant concerns about lifetime. As HOT detectors and TE coolers continue to improve, it may become possible to eliminate cryocoolers from the CMIS design.

This paper provided strong evidence that a low-cost constellation of CubeSats is capable of providing stereo observations needed for accurate, precise retrievals of global CTHs and AMVs. Despite the challenges associated with turbulence and course corrections for an aircraft, the CMIS instrument demonstrated excellent accuracy for CTHs and AMVs with standard deviations of 20.2 m and 0.23 m s^{-1}, respectively, for idealized collections against stationary terrain. For a case which the Gulfstream-III underflew both GOES and Aeolus, CMIS provided reasonable results. The success of the aircraft retrievals suggests that even better results would be achieved from space.

Author Contributions: Conceptualization, Michael Kelly and Dong Wu.; methodology, Michael Kelly, James Carr and Arnold Goldberg.; software, James Carr and Ivan Papusha; validation, James Carr, Dong Wu, and Arnold Goldberg; formal analysis, James Carr, Arnold Goldberg, and Renee Meinhold; investigation, Michael Kelly and Arnold Goldberg.; resources, Michael Kelly.; data curation, Ivan Papusha and Renee Meinhold.; writing—original draft preparation, Michael Kelly, James Carr, and Dong Wu.; writing—review and editing, Michael Kelly, James Carr, Arnold Goldberg, and Dong Wu.; visualization, James Carr, Dong Wu, Ivan Papusha, Renee Meinhold.; supervision, Michael Kelly.; project administration, Michael Kelly; funding acquisition, Michael Kelly

Funding: This research was funded by NASA Earth Science Technology Office Instrument Incubator Program (IIP), grant number NNX17AG65G.

Data Availability Statement: Data from the case studies can be made available upon request to the corresponding author.

Conflicts of Interest: The authors declare no conflict of interest.

References

1. Santek, D.; Dworak, R.; Nebuda, S.; Wanzong, S.; Borde, R.; Genkova, I.; García-Pereda, J.; Galante Negri, R.; Carranza, M.; Nonaka, K.; Shimoji, K.; Oh, S.M.; Lee, B.-I.; Chung, S.-R.; Daniels, J.; Bresky, W. 2018 Atmospheric Motion Vector (AMV) Intercomparison Study. *Remote Sens.* **2019**, *11*, 2240. https://doi.org/10.3390/rs11192240
2. National Academies of Sciences, Engineering, and Medicine. *Thriving on Our Changing Planet: A Decadal Strategy for Earth Observation from Space*, The National Academies Press: Washington, DC, USA **2018**; pp. 717, https://doi.org.10.17226/24938.
3. Zeng, X.; Ackerman, S.; Ferraro, R.D.; Lee, T.J.; Murray, J.J.; Pawson, S.; Reynolds, C.; Teixeira, J. Challenges and opportunities in NASA weather research. *Bul. Amer. Met. Soc*., **2016**, *97(7)*, ES137-ES140. https://doi.org/10.1175/BAMS-D-15-00195.1
4. Carr, J.L.; Wu, D.L.; Kelly, M.A.; Gong, J. MISR-GOES 3D Winds: Implications for Future LEO-GEO and LEO-LEO Winds, *Remote Sens.* **2018**, *10 (12)*, 188
5. Wertz, J.R.; Larson, W.J., eds. *Space mission analysis and design*, 3rd ed.; Microcosm: Hawthorne, CA, USA, 2010 p. 135.
6. Liu, Q.; Ignatov, A.; Weng, F. Removing solar radiative effect from VIIRS M12 Band at 3.7 μm for daytime sea surface temperature retrievals. *J. Atmos. Ocean. Tech*. **2014**, *31*, 2522-2529. DOI: 10.1175/JTECH-D-14-00051.1
7. Carr, J.L.; Wu, D.L.; Daniels, J.; Friberg, M.D.; Bresky, W.; Madani, H. GEO–GEO Stereo-Tracking of Atmospheric Motion Vectors (AMVs) from the Geostationary Ring. *Remote Sens*. **2020**, *12*, 3779. https://doi.org/10.3390/rs12223779
8. Stark, B.; McGee, M.; Chen, Y. Short wave infrared (SWIR) imaging systems using small Unmanned Aerial Systems (sUAS), Proceedings of the 2015 International Conference on Unmanned Aircraft Systems (ICUAS), Denver, CO, USA, IEEE, June 10-12, 2015, pp. 495-501, https://doi.org/10.1109/ICUAS.2015.7152328.

9. Mueller, K. J.; Wu, D.; Horváth, L.; Jovanovic, Á.; Muller, V.M.; Di Girolamo, J.P.; et al. Assessment of MISR Cloud Motion Vectors (CMVs) Relative to GOES and MODIS Atmospheric Motion Vectors (AMVs). *J. Appl. Met. Clim.* **2017**, *56(3)*, 555–572.
10. Weisz, E.; Li, J.; Menzel, W. P.; Heidinger, A. K.; Kahn, B. H.; Liu, C.-Y. Comparison of AIRS, MODIS, CloudSat and CALIPSO cloud top height retrievals. *Geophys. Res. Lett.*, **2007**, *34*, L17811, doi:10.1029/2007GL030676.
11. Carr, J.L.; Wilson, C.; Wu, D.; French, M.; Kelly, M. An innovative spacecube application for atmospheric science, 2020 IEEE International Geoscience and Remote Sensing Symposium, 26 Sep-2 Oct 2020, pp. 3853-3856, https://doi.org/10.1109/IGARSS39084.2020.9324477
12. Witchas, B.; Lemmerz, C.; Geiß, A.; Lux, O.; Marksteiner, U.; Rahm, S.; Reitebuch, O.; Weiler, F. First validation of Aeolus wind observation by airborne Doppler wind lidar measurements. *Atmos. Meas. Tech*. **2020**, *13*, 2381-2396, https://doi.org/10.5194/amt-13-2381-2020
13. Holtslag, A. A. M.; F. T. M. Nieuwstadt, F.T.M. Scaling the atmospheric boundary layer. *Bound.-Layer Meteor.*, **1986**, *36*, 201–209.
14. Seibert, P.; Beyrich, F.; Gryning, S.E.; Joffre, S.; Rasmussen, A.; Tercier, P. Review and intercomparison of operational methods for the determination of the mixing height. *Atmos. Environ.*, **2000**, *34*, 1001–1027.
15. Stevens, B. Entrainment in stratocumulus topped mixed layers. *Quart. J. Roy. Meteor. Soc.*, **2002**, *128*, 2663–2689.
16. Lin, J.-T.; Youn, D.; Liang, X.-Z.; Wuebbles, D. J. Global model simulation of summertime U.S. ozone diurnal cycle and its sensitivity to PBL mixing, spatial resolution, and emissions. *Atmos. Environ.*, **2008**, *42*, 8470–8483.
17. Konor, C. S.; Boezio, G.C.; Mechoso, C. R.; Arakawa, A. Parameterization of PBL processes in an atmospheric general circulation model: Description and preliminary assessment. *Mon. Wea. Rev.*, **2009**, *137*, 1061–1082.
18. Wood, R.; Bretherton, C. S. Boundary layer depth, entrainment and decoupling in the cloud-capped subtropical and tropical marine boundary layer. *J. Climate*, **2004**, *17*, 3575-3587.
19. Zuidema, P.; Painemal, D.; de Szoeke, S.; Fairall, C. Stratocumulus cloud-top height estimates and their climatic implications, *J. Clim.*, **2009**, *22(17)*, 4652–4666.
20. Kollias, P.; Albrecht, B. The Turbulence Structure in a Continental Stratocumulus Cloud from Millimeter-Wavelength Radar Observations. *J. Atmos Sci*. **2000**, *57*, 2417-2434. https://doi.org/10.1175/1520-0469(2000)057<2417:TTSIAC>2.0.CO;2
21. Intrieri, J. M.; Shupe, M. D.; Uttal, T.; McCarty, B. J. An annual cycle of Arctic cloud characteristics observed by radar and lidar at SHEBA. *J. Geophys. Res.*, **2002**, *107*, 8030, https://doi.org/10.1029/2000JC000423
22. Karlsson, J.; Svensson, G.; Cardoso, S.; Teixeira, J.; Paradise, S. Subtropical cloud-regime transitions. Boundary-layer depth and cloud-top height evolution in models and observations. *J. Appl. Met. Clim.* **2010**, *49*, 1845-1858. https://doi.org/10.1175/2010JAMC2338.1
23. Kay, J. E.; L'Ecuyer, T.; Gettelman, A.; Stephens, G.; O'Dell, C. The contribution of cloud and radiation anomalies to the 2007 Arctic sea ice extent minimum, *Geophys. Res. Lett.*, **2008**, *35*, L08503, https://doi.org/10.1029/2008GL033451.
24. Wu, D.L; Lee, J.N. Arctic Low Cloud Changes as Observed by MISR and CALIOP: Implication for the enhanced autumnal warming and sea ice loss. *J. Geophys. Res*. **2012**, *117*, D07107. https://doi.org/10.1029/2011/D017050.
25. Carr, J.L.; Wu, D.L.; Wolfe, R.E.; Madani, H.; Lin, G.; Tan, B. Joint 3D-Wind Retrievals with Stereoscopic Views from MODIS and GOES. *Remote Sensing*, **2019**, *11(18)*, 2100. https://doi.org/10.3390/rs11182100